Supporting Information

Deciphering the Dynamic Structure Evolution of Fe and Ni Co-doped CoS_2 for Enhanced Water Oxidation

Wenfeng Peng, †[a] Amol Deshmukh, †[b] Ning Chen,[c] Zhengxing Lv,[d] Shijing Zhao,[a] Jiong Li,[d] Bingmin Yan,[a] Xiang Gao,[a] Lu Shang,[e] Yutong Gong,[f] Lailei Wu,*[g] Mingyang Chen,*[b,h,i] Tierui Zhang[e] and Huiyang Gou*[a]

[a] Center for High Pressure Science and Technology Advanced Research, Beijing 100094, China.

[b] Computational Science Research Center, Beijing 100193, China.

[c] Canada Canadian Light Source Saskatoon, Saskatchewan S7N2V3, Canada.

[d] Shanghai Synchrotron Radiation Facility, Shanghai, 201210, China.

[e] Key Laboratory of Photochemical Conversion and Optoelectronic Materials, Technical Institute of Physics and Chemistry, Chinese Academy of Sciences, Beijing 100190, China.

[f] State Key Laboratory of Solidification Processing, Northwestern Polytechnical University, Xi'an, Shaanxi 710072, China.

[g] Yanshan University, Qinhuangdao 066004, China.

[h] Center for Green Innovation, School of Materials Science and Engineering, University of Science and Technology Beijing, Beijing 100083, China.

[i] Shunde Graduate School of University of Science and Technology Beijing, Foshan 528000, China.

Corresponding Author

*wll@ysu.edu.cn

*mychen@ustb.edu.cn

*huiyang.gou@hpstar.ac.cn

Experimental section

1. Chemicals

Cobalt nanopowder (purity, 99.99%), Nickel nanopowder (purity, 99.99%), iron nanopowder (purity, 99.99%) and sulfur powder (purity, 99.99%) were from Aladdin Chemical Co., Ltd. Potassium hydroxide (KOH, AR; density, 2.130 $g \cdot cm^{-2}$) and Nafion binder (Nafion D-521 dispersion, 5% w/w in water and 1-propanol, ≥0.92 meq/g exchange capacity) were from Tianjin Kemiou Chemical Reagent Co., Ltd.

2. Electrocatalysts synthesis

$Co_{0.8}Fe_{0.11}Ni_{0.09}S_2$ (henceforth referred to as Fe,Ni-CoS_2), $Co_{0.8}Fe_{0.2}S_2$ (henceforth referred to as Fe-CoS_2), $Co_{0.8}Ni_{0.2}S_2$ (henceforth referred to as Ni-CoS_2), CoS_2, FeS_2, and NiS_2 were synthesized by the high temperature and high pressure (HTHP) process in a cubic multi-anvil device (CS−1B type, Guilin, China). Pyrophyllite pressure medium, a graphite heater, and an h-BN capsule were included in the assemblies. W-Re (type C) thermocouples were used to calibrate the temperature. The following are the typical synthetic steps: First, in a glove box, the stoichiometric Co, Fe, Ni and S powders for Fe,Ni-CoS_2, Fe-CoS_2, Ni-CoS_2, CoS_2, FeS_2, and NiS_2 are mixed by hand using agate mortar and pestle no less than 30 min. The mixtures are then pre-pressed at 20 MPa into a cylindrical block precursor (five millimeters by three millimeters) and encapsulated into h-BN capsules. Finally, the samples are heated to 1500 °C under 5.0 GPa for 15 min. The ultrafine powder was obtained through the high-energy mechanical milling method. All of the samples were ball-milled for 10 hours under Ar atmosphere using a planetary-type high energy ball mill with a ball to power ratio of 20:1 at 350 rpm.

3. Morphology and structure analysis

X-ray diffraction (XRD) patterns of the synthetic electrocatalyst were obtained by a PANalytical X'Pert Pro X-ray diffractometer with Cu Kα radiation (λ = 0.15406 nm) at a scan

rate of 0.013° min^{-1}. Their morphology was characterized by the field emission scanning electron microscopy (FESEM, JSM-7900F) and transmission electron microscopy (TEM&HRTEM, JEOL2010, Japan) equipped with X-ray energy-dispersive spectroscopy detector (EDS). And the element mapping and high-resolution TEM (HRTEM) were carried out at 200 kV. X-ray photoelectron spectroscopy (XPS, AXIS Ultra DLD, Japan) with a monochromatic Al Kα X-ray source is used to determine the chemical states of the elements. All operando Raman measurements were carried out using a custom-built spectro-electrochemical cell. The electrochemical reactions were monitored by an electrochemical workstation (CHI760E) in a three-electrode configuration (1M KOH). The Pt wire and Ag/AgCl electrode were used as the counter electrode and the reference electrode, respectively. The working electrodes were prepared by drop-casting the ink (the mixture of 1ml ethanol, 30 μL Nafion and 4 mg electrocatalysts was sonicated over 30 min) on a specially designed glass carbon electrode (diameter is 6 mm) and the mass density of catalyst is about 0.24 mg cm^{-2}. The in-situ and ex-situ Raman spectra were acquired using confocal micro-Raman spectroscopy (LabRam HR Evolution, Horiba) equipped with a 532 nm laser excitation and an 1800 lines/mm grating monochromator. And each spectrum was acquired in 30 s with 3 sweeps from 100 to 1000 cm^{-1}.

Samples for operando XAS measurements were conducted in a custom-made in-situ electrochemical cell under the fluorescence model. The custom-made Teflon container (Figure S11a-b) with a specially designed window sealed by Kapton tape, which prevents any leakage of electrolyte and allows X-rays beam to pass. The carbon rod and Hg/HgO electrode were used as the counter electrode and the reference electrode, respectively. The working electrodes were prepared by drop-casting the ink (the mixture of 1ml ethanol, 30 μL Nafion and 4 mg electrocatalysts was sonicated over 30 min) on carbon paper (thickness was about 500 nm), which was fixed by Kapton tape. The operando electrochemical measurements were conducted on a computer-controlled electrochemical analyzer. At each potential, the catalyst was allowed

to be stabilized 10 min before XAS measurement and the potential was kept constant throughout the XAS measurement. Furthermore, the data for XAS was obtained at Beamline 11B Shanghai Synchrotron Radiation Facility (SSRF) and Hard X-ray MicroAnalysis (HXMA) beamline Light Source in Canadian (CLS). The storage ring is operated at 250 mA mode with a Si (111) double crystal monochromator to produce Monochromatic X-rays. The energy calibrations of the monochromator are checked by K-edge of Co foil (7709 eV), Fe foil (7112 eV) and Ni foil (8333 eV), respectively. All XAS data were processed using the ATHENA program of IFEFFIT software packages and analyzed in the WINXAS software.

4. Electrode preparations.

All working electrodes were made by using the following procedure. The catalyst ink was prepared by mixing 1ml ethanol, 30 μL Nafion and 4 mg as-prepared sulfide catalysts then ultrasound treating over 30 min. Then, the as-prepared catalyst suspension of 12 μL was drop-casted on the surface of the glass carbon electrode (GCE, 5.0 mm in diameter), yielding a catalyst mass density of 0.24 mg cm^{-2}. Finally, the catalyst-coated working electrodes were dried in the air for over 30 min. For preparation of nickel foam (NF)-supported working electrodes, first NF (geometric effective dimensioning:1x1 cm) were rinsed in ethanol under ultrasound for over 30 min and then dried. The as-prepared catalyst suspension was drop-casted on the support and the loading mass is about 4.0 mg. Finally, these catalyst-coated working electrodes were dried in the air over 5 h.

5. Electrochemical measurements

All electrochemical measurements are carried out at room temperature on an electrochemical workstation (CHI760E), with a typical three-electrode electrochemical system. The typical three-electrode electrochemical system consisting the working electrode, Hg/HgO (1.0 M KOH) reference electrode, and platinum counter electrode (1x1 cm). All of the tests were carried out in a 1.0 M KOH electrolyte.

All measured potentials were translated to the reversible hydrogen electrode (RHE) as follows:

$$E(RHE) = E(Hg/HgO) + 0.098 + 0.059 \times pH \quad (1)$$

And the overpotential is determined by the formula:

$$\eta = E(RHE) - 1.23\,V \quad (2)$$

Linear sweep voltammetry (LSV) curves were collected at a scan rate of 5 mV s^{-1} with 85% *iR*-compensation. Tafel slopes were determined by fitting the linear portion of the Tafel plots of the Tafel equation:

$$\eta = b * log(j) + a \quad (3)$$

Electrochemical impedance spectroscopy (EIS) tests were carried out at 0.6 V (vs. SCE) in a frequency range from 100k Hz to 0.01 Hz.

Cyclic voltammograms (CV) cures are measured at different scan rates (v=20, 40, 60, 80, and 100 mV s^{-1}) in the non-Faradic potential range of 0.05 to 0.1 V (vs. RHE).

The mass activity (MA) is calculated by the equation:

$$\text{MA} = j/m \quad (4)$$

Where, j is the current density (mA/cm^2), and m is mass density (mg/cm^2). And m is 0.24 mg/cm^2 in this work.

The following equation was used to evaluate the turnover frequency (TOF) of electrocatalysts:

$$\text{TOF} = (j \times A)/(4 \times F \times n) \quad (5)$$

Where j is the current density at a given overpotential, A is the electrode's surface area, 4 is the number of electrons transferred to produce one mole of O_2, F is the Faraday constant, and n is the number of moles of metal ions in the working electrode.

RRDE experiments were carried out using a CHI760E Electrochemical workstation, a speed control unit (1600 r.p.m.; Princeton Applied Research Model 636 Electrode Rotator) and a Ring disc electrode (GC and Pt ring, Figure S9c). The counter and reference electrodes are graphite rod and Ag/AgCl electrode, respectively. In addition, to reduce the O_2 produced by the catalyst in 1 M KOH, the ring potential was maintained at 0.4 V vs. RHE.

The FE was calculated as follow:

$$\mathrm{FE} = I_{ring}/(I_{disk}N) \quad (6)$$

Where, I_{ring}, I_{disk} and N are ring current, disk current, and current collection efficiency, respectively. And the N in here is 0.2.

The chronoamperometric test is carried out with an initial current density of 52 $\mathrm{mA \cdot cm^{-2}}$ (the samples are deposited on the nickel foam electrode). The materials (deposited on carbon cloth) are measured in the CV model at a rate of 100mV/s from 1.23V vs. RHE to the potential where the current density is 100 $\mathrm{mA/cm^2}$, after two hours' reaction, the samples are collected defined as after OER.

6. Particle size effect on XAS modeling

Notice that what the structural systems intend to reproduce is a sub-nano to nanoscale decomposition process of Fe,Ni-CoS_2 type of structure throughout the in-situ process versus the in-step growth of CoOOH type of structure in the system in roughly the same scale. The corresponding XANES modeling upon structure systems is to correlate the particle size effect described by structure systems to data trends resolved experimentally by XANES. Here cluster radii specified for cluster components of two structure systems are regarding as the kernel portion of the corresponding particle which possesses the corresponding Fe,Ni-CoS_2 and CoOOH types of Co local structure structures. The size of actual particles of Co clusters in the sample may be larger than the corresponding specified clusters defined by structure systems if having surface attached atoms considered. But since positions of those surface attached atoms are often displaced away from the corresponding crystallography prediction because of surface effect, their XAFS backscattering is expected to experience a cancellation effect among surface atoms, making XANES from particle surface atoms only has a secondary effect on the overall XANES. Therefore, XANES contribution from a surface atom is ignored, only the kernel

portion of particles which possess Fe,Ni-CoS_2 and CoOOH types of structures are considered in the reported modeling.

The modeling also reveals a significant increase in the relative intensity of feature "B" and substantial peak drifting and relative intensity increasing of feature "C" from clusters R3Å to R4Å. Notice that the structure changing of CoOOH clusters from R3Å to R4Å corresponds to a critical point of CoOOH structure extension from 2D to the 3D framework. Notice that CoOOH structure is featured by CoO_6 octahedron sheets bridged by hydrogen sheets in between (Figure S14). For cluster R⩽3Å, CoOOH possessed a flake type of particle morphology. For cluster R=4Å, Co begins to see the oxygen belonging to neighbored CoO_6 octahedron sheets, namely CoOOH type of structure begin to extend from 2D flake type of morphology to 3D. For cluster R⩾5Å, the CoOOH type structure domain grows up to nanoscale particle or lager, reaching the XANES detecting limit with the intensity of "C" saturated.

7. Possible error analysis in LCF

Possible error in LCF analysis induced by using these two standard spectra still needs to be addressed considering at first that two XANES standard spectra were obtained from model compound samples long-range ordered, secondly XANES theoretical modeling has revealed particle size effect may impact XANES of both Co species (Figure S25-26), and thirdly the CoOOH type of Co structure did expect to grow throughout the *in-situ* process.

From Fe,Ni-CoS_2 XANES perspective, theoretical modeling revealed that the size effect constrains to particles with size ranged R≤6Å, featured by changing in intensity and drifting of peak position ("A" in Figure S25). But the peak drifting of the feature is not experimentally resolved by the in-situ data system ("A", Figure 3c), indicating that Fe,Ni-CoS_2 particles in the sample system were constantly ranged R≥6Å throughout the in-situ reaction. Therefore Fe,Ni-CoS_2-Co-OCP is an ideal standard for LCF analysis. From CoOOH XANES perspective, small error is expected for LCF by using the standard spectrum from the model compound CoOOH,

induced by particle size effect upon features “B” and “C” (Figure S26). The size effect of “B” is featured mainly as changing in the peak relative intensity and secondly as peak broadening. This broadening effect of “B” is further associated with the peak drifting and line broadening of “C”. The XANES modeling also reveals that the effects to “B” and “C” are both mostly constrained to CoOOH particles with size ranged R≤4Å in radius, and almost completely ignorable for particles size ranged R≥4Å. Even for particles ranged R≤4Å, the overall size effect induced intensity changing is rather small, counting for only a few percent of XANES signal of the data region.

Therefore, CoOOH size effect related LCF analysis error is expected to be ignorable for this in-situ data system, considering at first that the largest possible size related error from CoOOH standard spectrum is expected at the low voltage end of the in-situ reaction, e.g., Fe,Ni-CoS_2-Co-1.1 V. The CoOOH in the sample at this reaction condition is anticipated still at its precursor development stage for CoOOH structure, e.g., growth from 2D flake to 3D CoOOH type of structure domain (Figure S24). At this stage the intensity of “B” and “C” of the standard spectrum might be slightly overemphasized for the CoOOH type of structure in the sample. However, the estimated weight of CoOOH at this stage is a minor level of ~ 3% level (Table S7). Considering that the underestimation of CoOOH weight induced by overemphasizing the signal intensity at “B” and “C” from the standard spectrum is only a few percent of the overall CoOOH XANES signal, the error induced by the “B” and “C” size effect at this amount of CoOOH, i.e. 3%, is less than 0.1% for total XANES signal, thus the error is ignorable even at this data point regarding the overall LCF result. Secondly, XANES modeling further indicates that features “B” and “C” induced LCF error can be completely ignored for rest data points of the in-situ data system with progressively increasing voltage, considering that “B” and “C” quickly reach their peak status when CoOOH structure domain grows up to Nana scale (i.e., R ⩾4) (Figure S26).

8. Computational details.

All the density functional theory level first-principles calculations in this study were performed using Vienna Ab-initio Simulation Package (VASP).[1-2] The exchange correlation energies were approximated by using the Perdew, Burke, and Ernzerhof (PBE) functional.[3] The spin polarized electron wave functions expanded in plane wave basis sets with 500 eV energy cutoff and pseudopotentials were constructed with the projected augmented wave (PAW) method.[4] In addition, the DFT-D_3 correction proposed by Grimme is applied to include dispersion interactions.[5]

The cubic-phase CoS_2 crystal structure (space group: *Pa*-3) was first optimized until the forces on each relaxed atoms are smaller than 0.01 eV/Å. During the bulk calculations, the lattice parameters and atom positions were relaxed. The lattice parameter for the cubic CoS_2 is predicted as $a=b=c$=5.509 Å, which is in good agreement with the experiment.

OER reaction over (102) surface of pure CoS_2 and Fe and Ni doped CoS_2 were performed. The nonpolar (102) slab was cut from cubic-phase CoS_2 crystal structure and 1×2 supercell (12.312×11.012 $Å^2$) was created. The supercell contains 36 Co and 80 S atoms with a thickness of ~11 Å, which is approximately stoichiometric. A vacuum of 20 Å was placed between the slab images. Fe and Ni dopants were introduced to replace surface Co atoms, which create four doped CoS_2 (102) slabs, $Co_{35}FeS_2$, $Co_{35}NiS_2$, $Co_{34}NiFeS_2$-1, and $Co_{34}NiFeS_2$-2, labeled with the molecular formula of the supercell. $Co_{34}NiFeS_2$-1 and $Co_{34}NiFeS_2$-2 are two homotops for the Fe and Ni co-doped CoS_2 (102), where the relative position of the surface Fe and Ni dopants differs. For both cases, the Fe and Ni dopants are nearest neighbors connected by an S atom. For the slab optimization calculations, the lattice parameters of the optimized bulk systems were used and only the positions of the atoms were optimized. A vacuum of at least 20 Å was set for all the slab systems. A 1×2 Monkhorst-Pack K-point mesh was used in the DFT calculations.[6]

The OER reaction was modeled for the selected active sites, following the 4-electron (or 4-hole) mechanism proposed by Nørskov.[7]

$$OH^- + * \rightarrow *OH + e^- \quad (7)$$

$$*OH \rightarrow *O + H^+ + e^- \quad (8)$$

$$OH^- + *O \rightarrow *OOH + e^- \quad (9)$$

$$*OOH \rightarrow * + O_2 + H^+ + e^- \quad (10)$$

where the adsorbates including OH, O, and OOH are added to the active site of the slabs (*) and the reaction energies were calculated accordingly. Assembling the reaction energies for steps (7) to (10) gives the energy profile for OER at a particular site. Subtracting the reaction energies by 1.23 V for each elementary charge transfer reaction results in the reaction energy barriers under an external bias of 1.23 V and the theoretical overpotential η_{DFT} can be predicted by equation (11)

$$\eta_{DFT} = \max (\Delta E_S (1.23\ V)) \quad (11)$$

where S indicates an elementary reaction step.

Similarly, the Fe and Ni co-doped CoS_2 (011) and (111) slabs were constructed for OER profile analysis. The supercell for the Fe and Ni co-doped CoS_2 (011) has a size of 7.787×11.012×33.627 $Å^3$ (slab thickness is approximately 13 Å), comprising $Co_{30}FeNiS_{60}$. The supercell for the Fe and Ni co-doped CoS_2 (111) has a size of 15.574×15.574×29.017 $Å^3$ (slab thickness is approximately 9 Å), comprising $Co_{46}FeNiS_{96}$.

The bulk doped $Co_xNi_yFe_zS_2$ materials, x + y + z = 1, were optimized at the PBE level using supercells comprising 32 sulfide units, in order to see the influence of the dopant concentration and on the stability of the material. The optimization calculations were carried out with an 8×8×8 K-point mesh, during which the lattice parameters and the atom positions were fully relaxed till energy change is below 0.0002 eV and force change is below 0.002 eV/Å. The formation energy per sulfide unit E_{form} for $Co_xNi_yFe_zS_2$ can be evaluated using equation (12):

$$E_{form} = E(Co_xNi_yFe_zS_2) - x*E(CoS_2) - y*E(NiS_2) - z*E(FeS_2) \quad (12)$$

where $E(Co_xNi_yFe_zS_2)$, $E(CoS_2)$, $E(NiS_2)$, and $E(FeS_2)$ are the predicted energy per sulfide unit (MS_2) at the DFT level for $Co_xNi_yFe_zS_2$, CoS_2, NiS_2, and FeS_2, respectively. The lattice deformation of $Co_xNi_yFe_zS_2$ with respect to the CoS_2 lattice is defined by equation (13):

$$\text{deformation (\%)} = \left(\left(\frac{(abc)_{Co_xNi_yFe_zS_2}}{(abc)_{CoS_2}}\right)^{\frac{1}{3}} - 1\right) * 100 \quad (13)$$

where *a*, *b*, and *c* denote the lattice parameters.

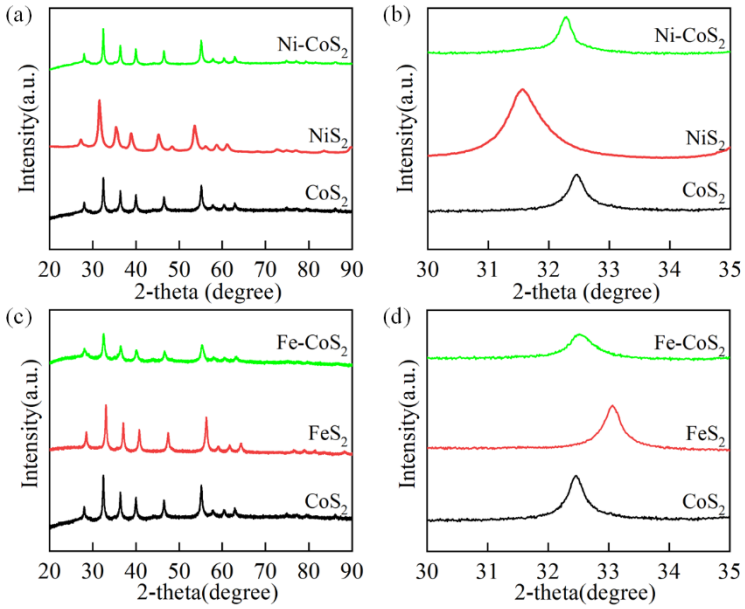

Figure S1: (a,c) Collected XRD patterns of Ni-CoS_2/NiS_2/CoS_2 and Fe-CoS_2/FeS_2/CoS_2 with pyrite structure; (b,d) their close look of (200) diffraction peak.

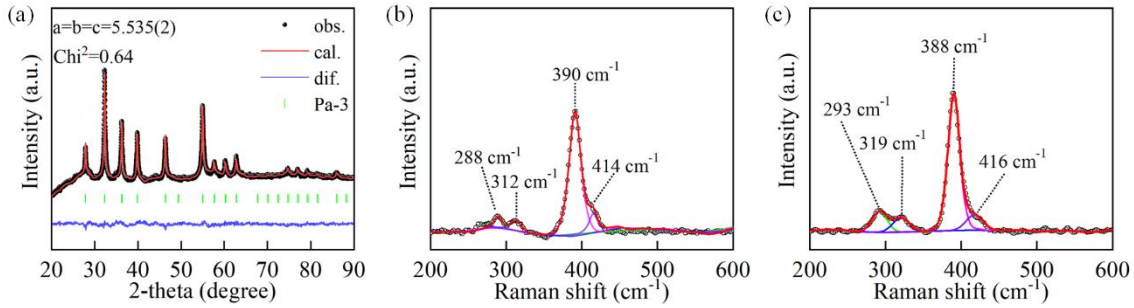

Figure S2: (a) Rietveld refinement of CoS_2. (b,c) the Raman fitting results of CoS_2 and Fe,Ni-CoS_2, respectively.

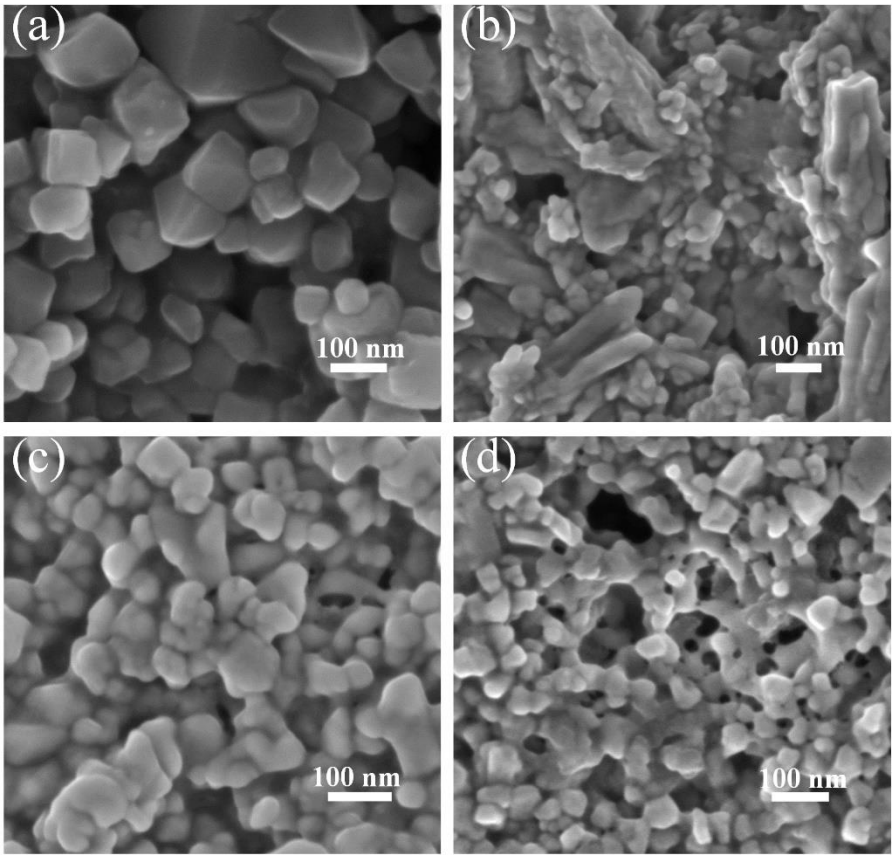

Figure S3: SEM images of CoS_2 (a), Ni-CoS_2 (b), Fe-CoS_2 (c) and Fe,Ni-CoS_2 (d) before OER.

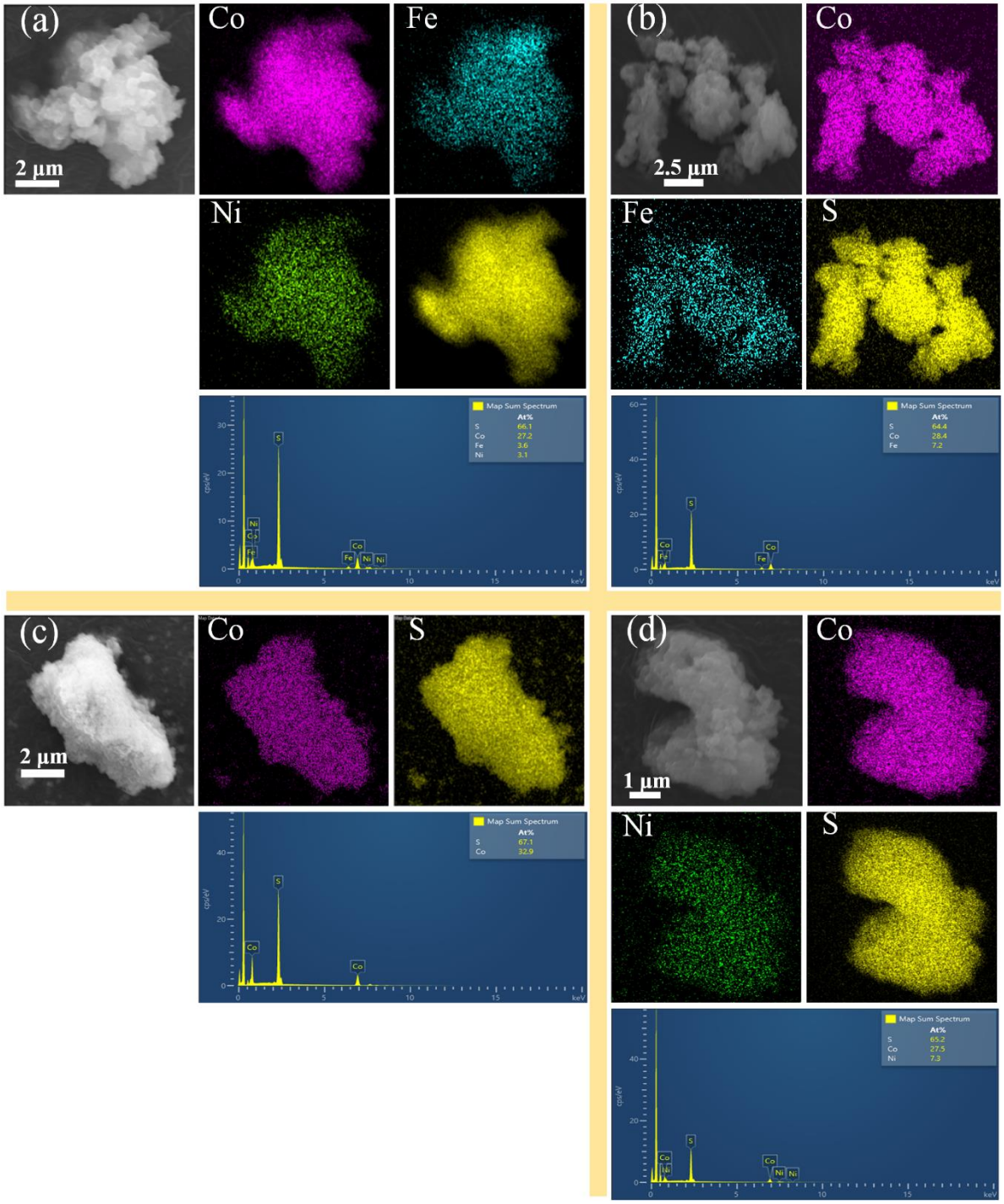

Figure S4: Energy dispersive X-ray (EDX) elemental mapping and corresponding FESEM−EDX spectra for Fe,Ni-CoS_2 (a), Fe-CoS_2 (b), CoS_2 (c) and Ni-CoS_2 (d).

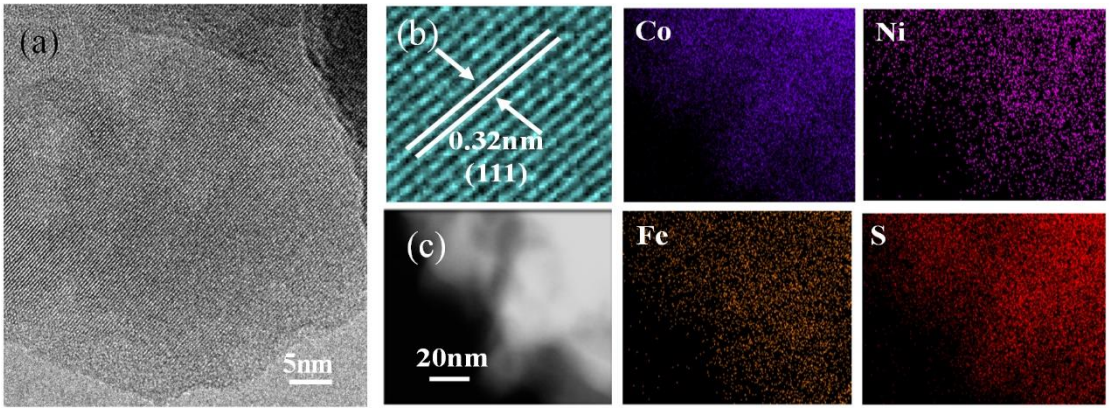

Figure S5: (a, b) HRTEM and its enlarged image of Fe,Ni-CoS_2 pre-catalyst. c) TEM-EDS mapping scans of Fe,Ni-CoS_2 catalyst.

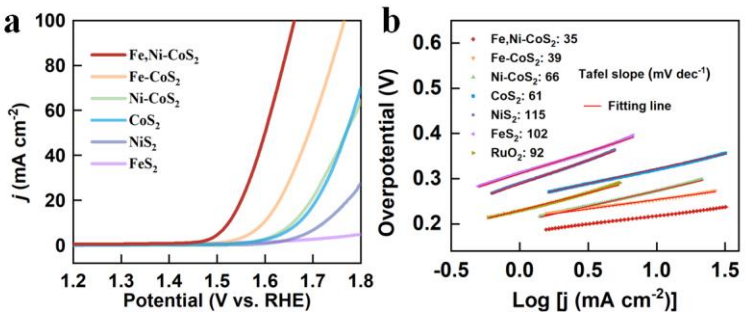

Figure S6: (a) no *iR*-corrected LSV curves of the as-prepared sulfides. (b) Tafel plots of as-prepared sulfide catalysts and RuO_2.

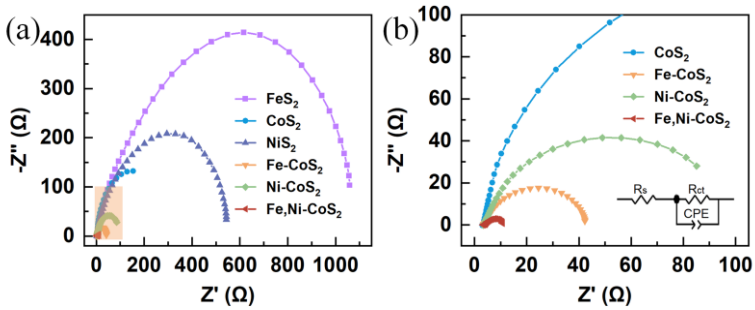

Figure S7: (a) Impedance curves of as-prepared sulfide electrocatalysts, (b) the partially enlarged view of (a). The equivalent circuit is embedded in (b).

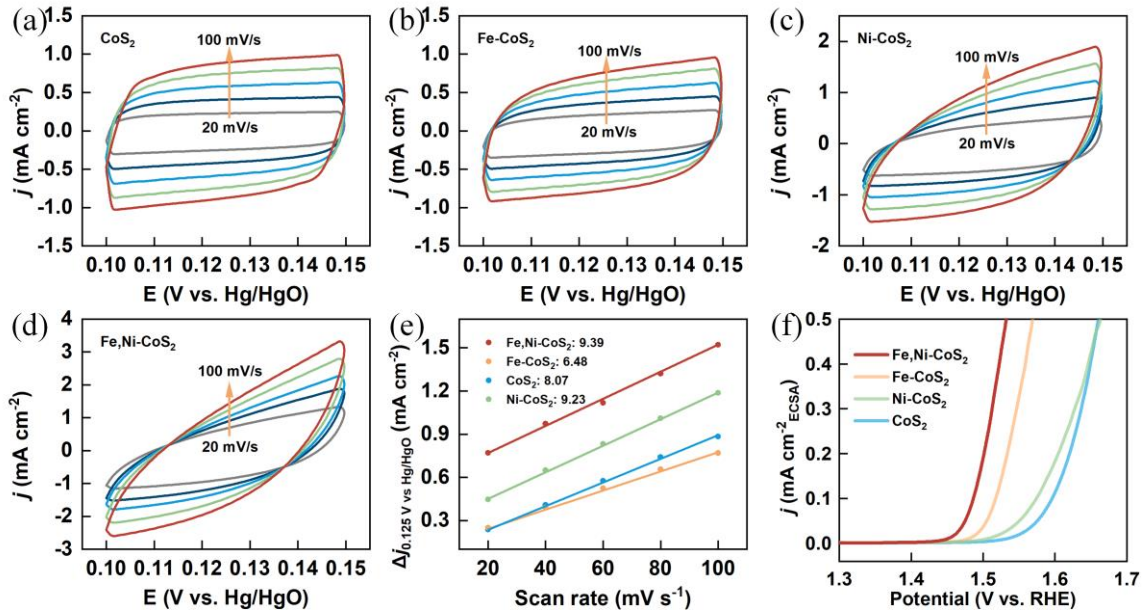

Figure S8: Electrochemical cyclic voltammograms (CVs) at different scanning rates of CoS_2 (a), Ni-CoS_2 (b), Fe-CoS_2 (c) and Fe,Ni-CoS_2 (d). (e) Double-layer capacitance (C_{dl}) of CoS_2, Ni-CoS_2, Fe-CoS_2 and Fe,Ni-CoS_2. (f) ECSA-normalized OER polarization curves of the fabricated sulfide catalysts.

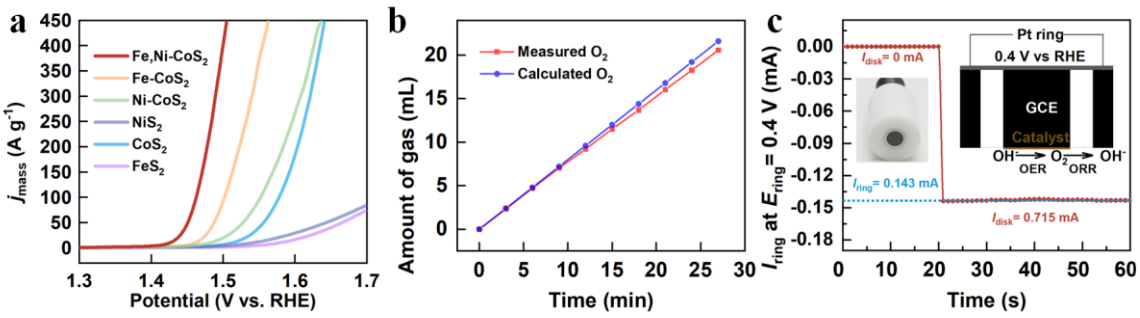

Figure S9: (a) the mass activity (MA) of the as-prepared sulfide electrocatalysts. The Faradaic efficiency for Fe,Ni-CoS_2 is determined by drainage method (b) and rotating ring-disk electrode (RRDE) measurement(c).

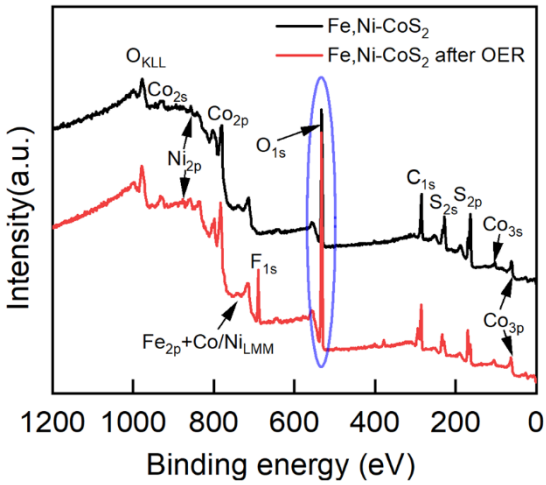

Figure S10: XPS survey spectra for Fe,Ni-CoS_2 before and after OER.

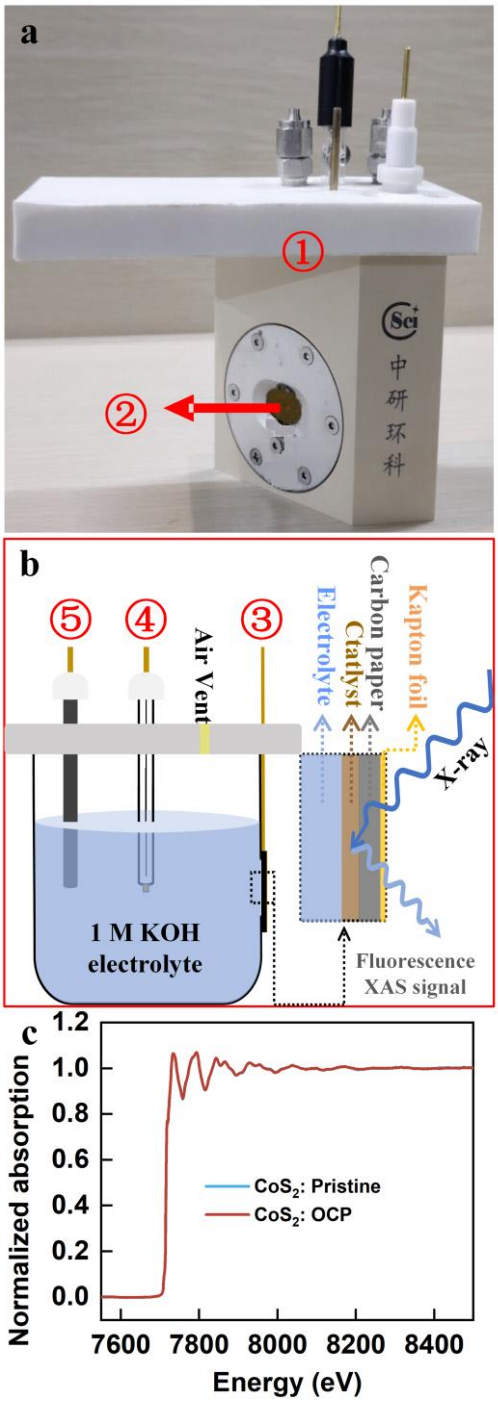

Figure S11: (a-b) The photo and its schematic configuration of the electrochemical cell for *operando* XAS setup experiments, respectively. ①in-situ electrochemical cell; ②kapton film; ③working electrode; ④reference electrode (Hg/HgO); ⑤counter electrode (carbon rod); ⑥ post-ionization chamber; ⑦Lytle type detector for collecting the fluorescence signals. (c) The XAS comparison of "Fe,Ni-CoS_2:Pristine" and "Fe,Ni-CoS_2:OCP" (immersion into the 1.0 M KOH electrolyte 30 min) show no obvious changes.

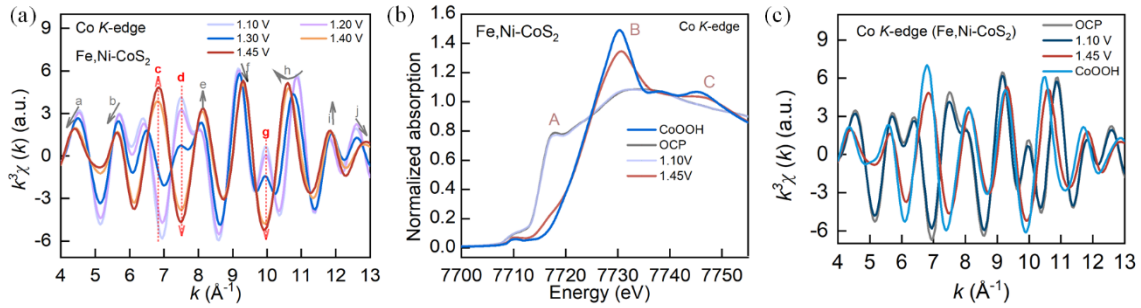

Figure S12: (a) FT filtered Co *K*-edge EXAFS $k^3\chi$(k) for Fe,Ni-CoS_2 at various applied potentials. Co *K*-edge XANES spectra (b) and EXAFS $k^3\chi(k)$ (c) of Fe,Ni-CoS_2 under different conditions (immersion into the 1.0 M KOH electrolyte 30 min, 1.1 V, and 1.45 V), and CoOOH.

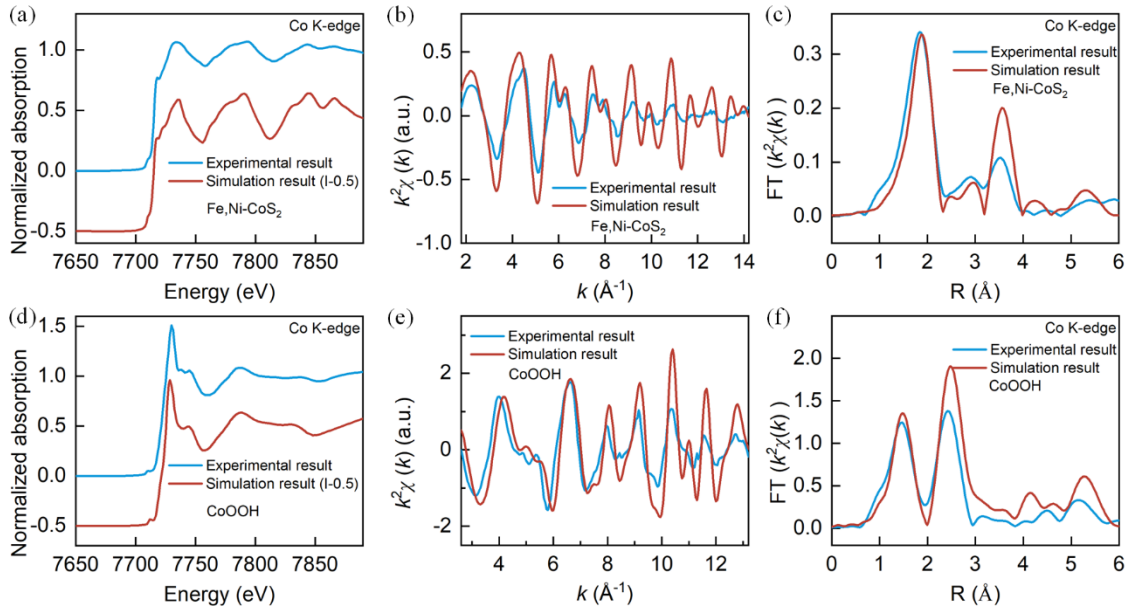

Figure S13: Comparison of experimental and theoretical simulation results (XANES, EXAFS in *k* space and R space) for Fe,Ni-CoS_2 and CoOOH, respectively. XAS modeling was performed upon Co centered spherical clusters with cluster radius up to 7Å for Fe,Ni-CoS_2 (ICSD-100325) and 6Å for CoOOH (COD, data-9009884), respectively.

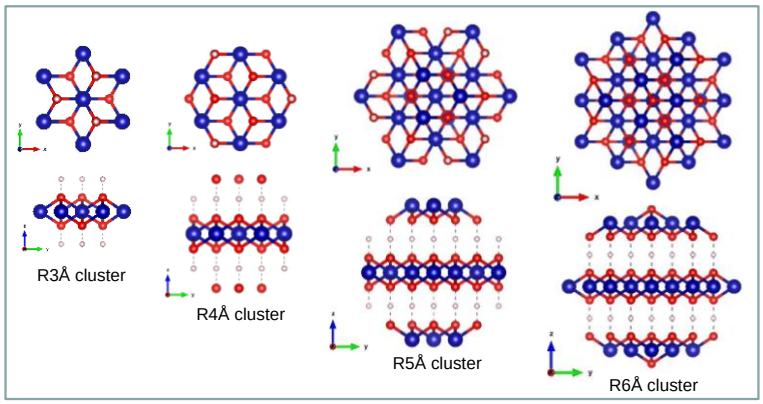

Figure S14: Co centered spherical cluster system was developed based on the structure of CoOOH (COD-9009884), i.e., R3.0, 4.0, 5.0 and 6.0Å.

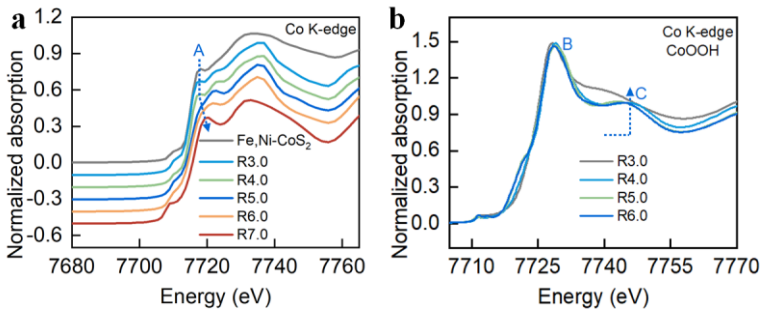

Figure S15: (a) XANES theoretical Fe,Ni-CoS_2 system, A trend is featured as following: cluster R≥6Å, no cluster size dependency resolved by the modeling; Cluster R6-5Å is critical cluster size range with the trend of (1) signal intensity decreasing and (2) feature peak drifting beginning to be resolved; R≤5Å, the trend continued for intensity decreasing and peak drifting. (b) XANES theoretical CoOOH system, featured by the following: "B" is not cluster size dependent; C progressively changed following particle size changing, feature as following: C begins to be resolved at R3.0Å cluster with lower feature intensity at an energy ~3 eV lower vs the final position; Intensity of C increases quickly when cluster size is increased, reaching feature maximum when R≥5.0Å; In-step with the increasing of feature intensity, peak position drifting to the experimentally resolved final C position.

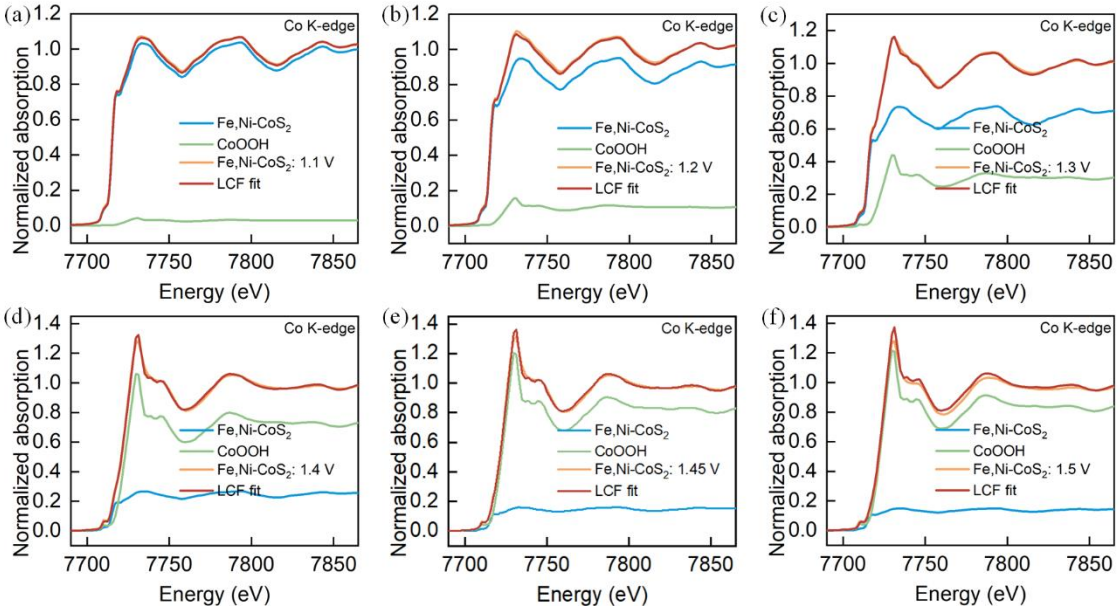

Figure S16: Comparison is made between ExpData, LCF fit, and two weighted standards throughout the redox process of the Fe,Ni-CoS_2 system.

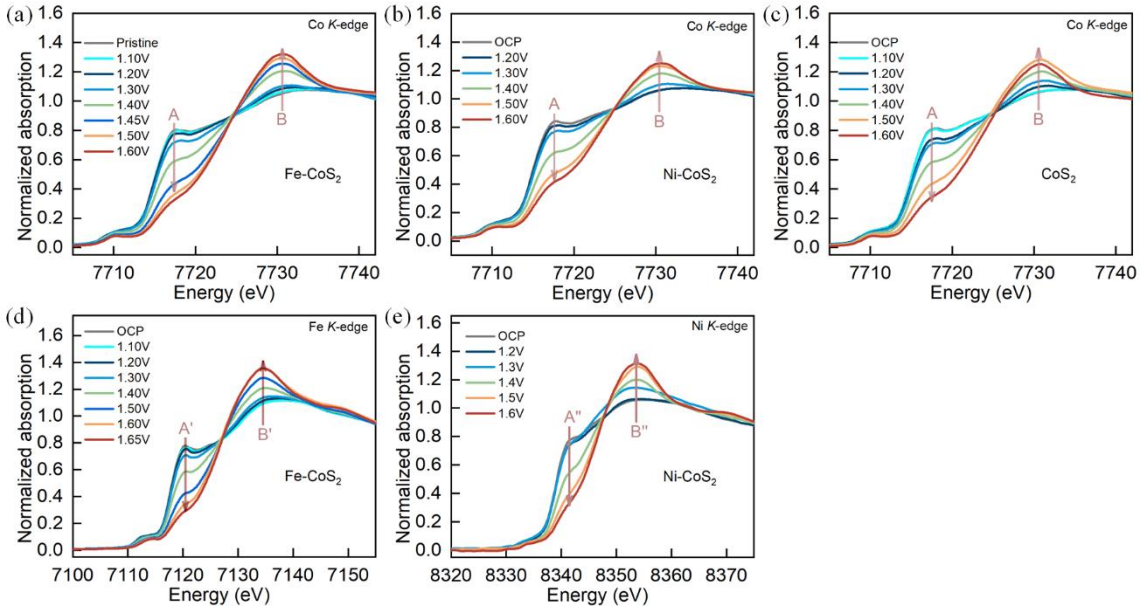

Figure S17: (a-c) *Operando* Co *K*-edge XANES spectra of Fe-CoS_2, Ni-CoS_2, and CoS_2 at varied potentials during the OER process, respectively. (d) *Operando* Fe *K*-edge XANES spectra of Fe-CoS_2 at varied potentials. (e) *Operando* Ni *K*-edge XANES spectra of Ni-CoS_2 at varied potentials.

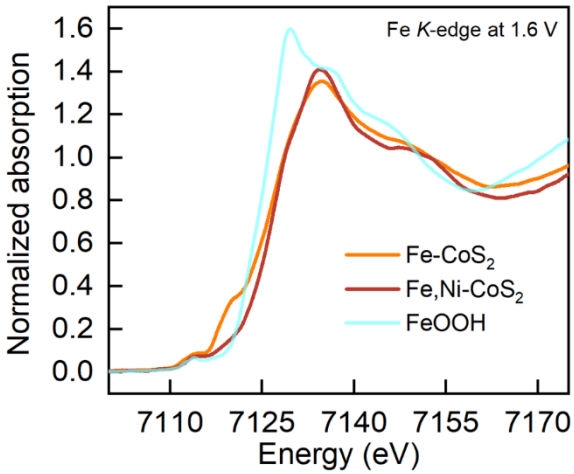

Figure S18: Comparison of Fe *K*-edge XANES spectra for Fe,Ni-CoS_2, Fe-CoS_2 at 1.6 V and FeOOH.

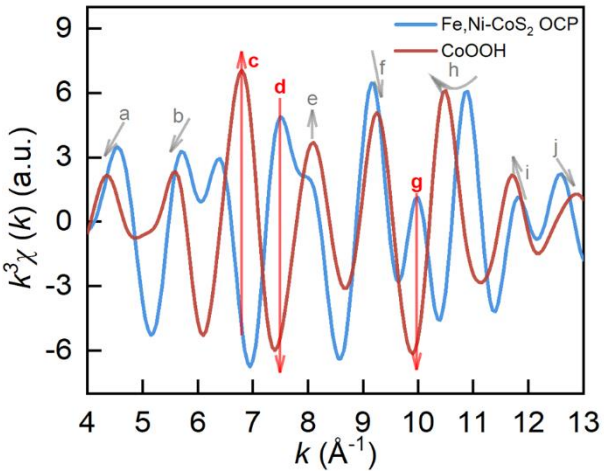

Figure S19: BFT-filtered Co *K*-edge EXAFS $k^3\chi(k)$ of Fe,Ni-CoS_2 OCP and CoOOH. The *k* space data range for forward Fourier transform and R space window for backward Fourier transform filtering were ranged between 2.6-13.9 $Å^{-1}$ and 1.0-5.6 Å, respectively. Sine window function was used for both forward and backward Fourier transform.

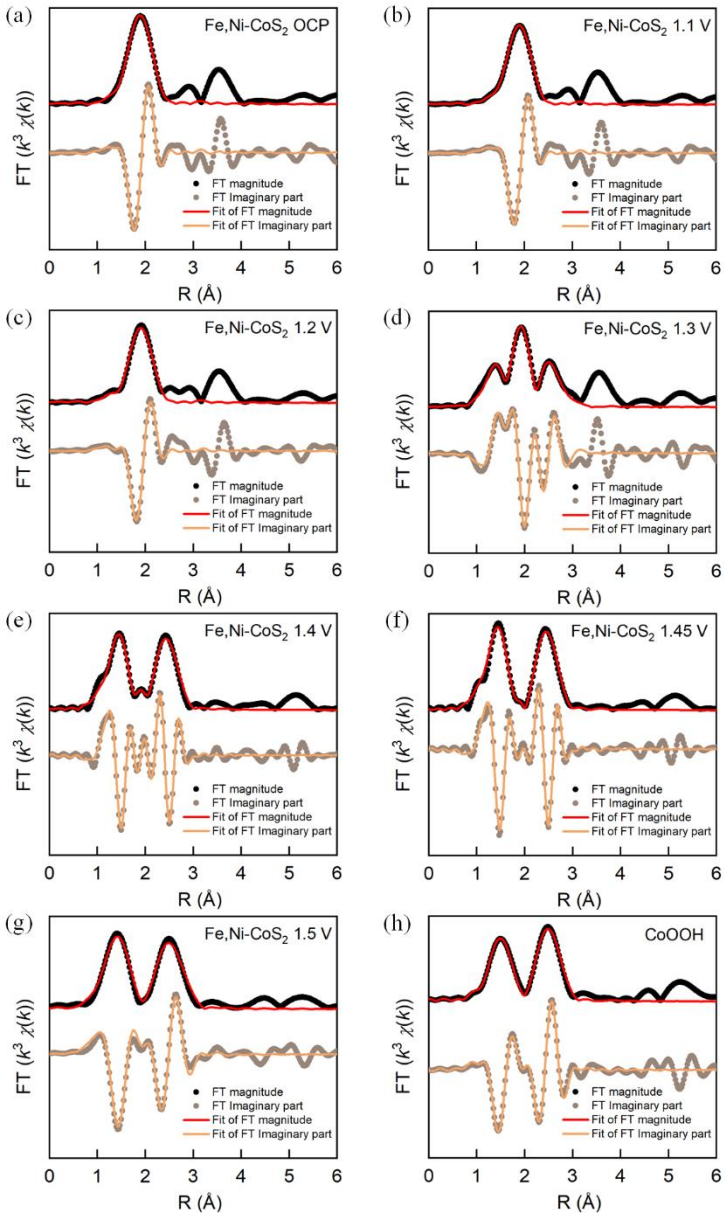

Figure S20: Fourier transformed k^3-weighted Co K edge EXAFS recorded for Fe,Ni-CoS_2 at open circuit potential (a), 1.1 V RHE anodic (b), 1.2 V RHE anodic (c), 1.3 V RHE anodic (d), 1.4 V RHE anodic (e), 1.45 V RHE anodic (f), 1.5 V RHE anodic (g) and CoOOH (h). experimental data (circle) and the corresponding fitting (line).

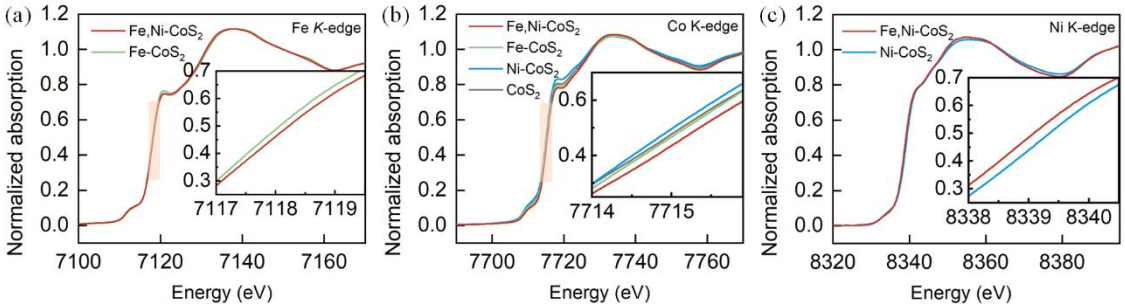

Figure S21: (a-c) Comparison of Fe, Co and Ni *K*-edge XANES spectra of Fe,Ni-CoS_2, Fe-CoS_2, Ni-CoS_2, and CoS_2, respectively.

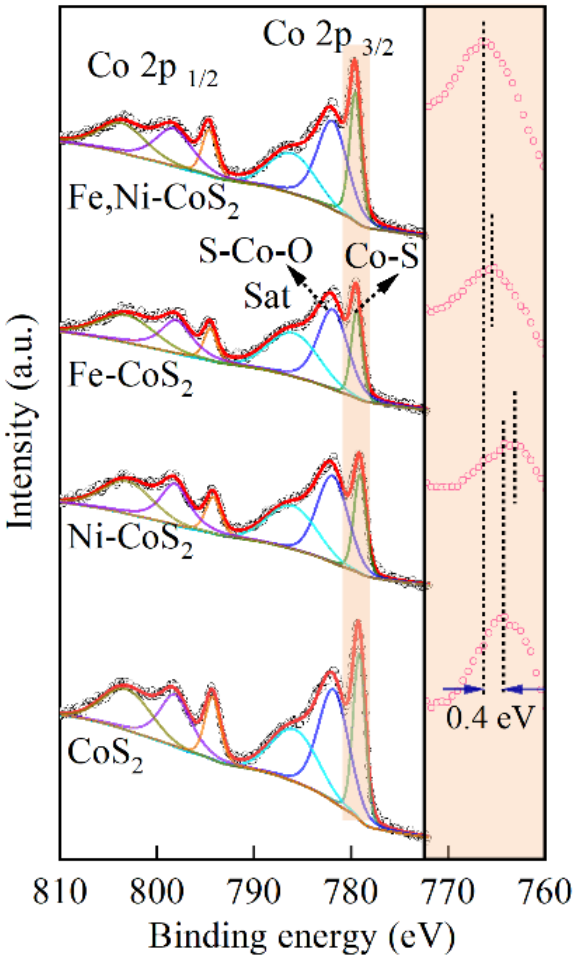

Figure S22: High-resolution XPS spectra of Co 2p for Fe,Ni-CoS_2, Fe-CoS_2, Ni-CoS_2 and CoS_2 before OER.

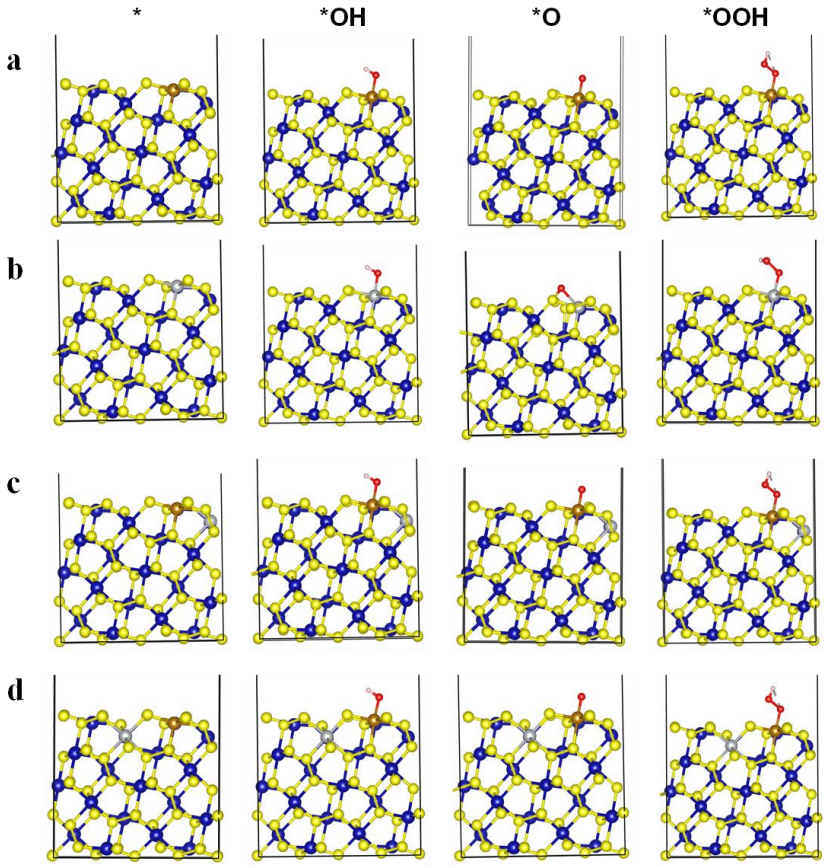

Figure S23: The *, *OH, *O, *OOH OER intermediates for the (102) surfaces of (a) Fe-doped CoS_2 (b) Ni-doped CoS_2 (c, d) Fe and Ni co-doped CoS_2 ($Co_{34}NiFeS_{80}$-1 and $Co_{34}NiFeS_{80}$-2 respectively).

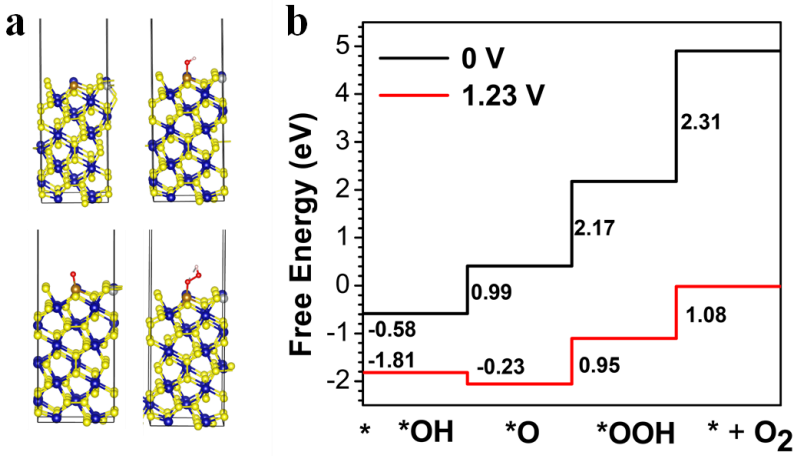

Figure S24. (a) The *, *OH, *O, and *OOH OER intermediates at the Fe site of the Fe and Ni co-doped CoS_2 (011) surface. (b) Calculated OER profiles at the DFT level for Fe site of the Fe and Ni co-doped CoS_2 (011) surfaces at an external bias of 0 V and 1.23 V.

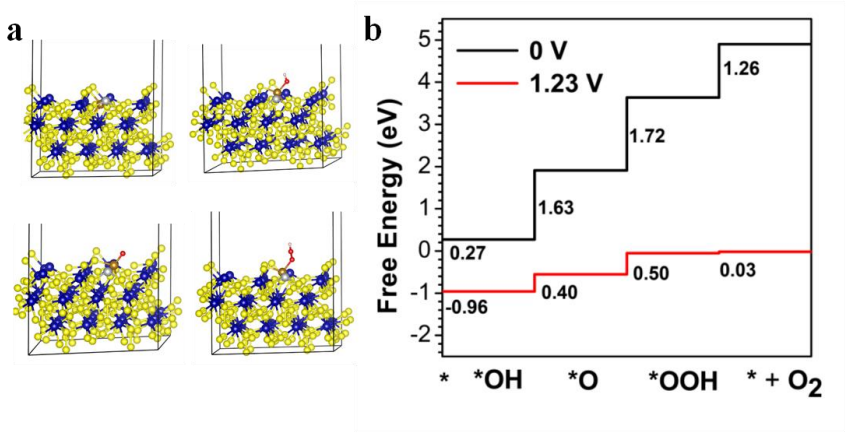

Figure S25. (a) The *, *OH, *O, and *OOH OER intermediates at the Fe site of the Fe and Ni co-doped CoS_2 (111) surface. (b) Calculated OER profiles at the DFT level for Fe site of the Fe and Ni co-doped CoS_2 (111) surfaces at an external bias of 0 V and 1.23 V.

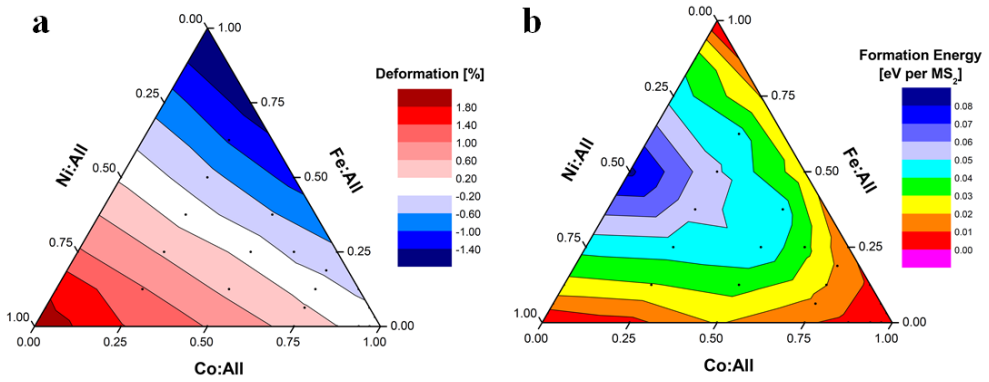

Figure S26. (a) Formation energy of $Co_xNi_yFe_zS_2$, x + y + z = 1, with respect to the pure MS_2. (b) The lattice parameter deformation (Δ(abc)1/3) for $Co_xNi_yFe_zS_2$ for the pure CoS_2.

Table S1: Crystal-structural parameters of the Fe,Ni-CoS_2 and CoS_2 from Rietveld refinement.

Composition		**Fe,Ni-CoS_2**	**CoS_2**
Space group		Pa-3 (205)	Pa-3 (205)
Phase structure		Cubic	Cubic
a=b=c (Å)		5.535	5.534
V ($Å^3$)		169.591	169.561
Z		4	4
Atom site	Co	(0.000, 0.000, 0.000)	(0.000, 0.000, 0.000)
	Fe	(0.000, 0.000, 0.000)	/
	Ni	(0.000, 0.000, 0.000)	/
	S	(0.389, 0.389, 0.389)	(0.388, 0.388, 0.388)

Table S2: Chemical compositions detected by the energy dispersive X-ray (EDX) elemental mapping.

Samples	Elenmets	Weight (wt%)	Atom (at%)
CoS_2	Co K	47.2	32.9
	S k	26.6	67.1
Ni-CoS_2	Co K	41.4	27.5
	Ni K	4.2	7.3
	S K	26.3	65.2
Fe-CoS_2	Co K	41.1	28.4
	Fe K	6.6	7.2
	S K	26.3	64.4
Fe,Ni-CoS_2	Co K	36.3	27.2
	Fe K	1.1	3.6
	NiK	27.5	3.1
	S K	26.4	66.1

Table S3: Comparison of OER electrocatalysts in 1.0 M KOH for similar reported systems.

Catalyst	mass density (mg cm^{-2})	j (mA cm^{-2})	η (mV)	Tafel slope (mV dec^{-1})	Electrolytes	Ref.
$Fe,Ni-CoS_2$	**0.24**	**10**	**242**	**35**	**1.0 M KOH**	**This work**
		100	**295**			
$CoFe_{0.2}S_x$	0.14	10	320	48.7	1.0 M KOH	[8]
B-TS-H@T-B	0.22	50	392.4	64	1.0 M KOH	[9]
ZnCoS-NSCNT/NP	0.21	10	270	73	1.0 M KOH	[10]
CoFeWS	0.21	10	286	38	1.0 M KOH	[11]
CoS-$Co(OH)_2$@MoS_{2+x}	0.20	10	410	68	1.0 M KOH	[12]
c-$FeCo_2S_y$/carbon	0.28	10	247	35	1.0 M KOH	[13]
CoS_2 MBs	0.50	10	308	41.4	1.0 M KOH	[14]
NiS_2/CoS_2/C	0.20	20	310	78	1.0 M KOH	[15]
Fe_3O_4@Co_9S_8/rGO-2	0.25	10	320	54.5	1.0 M KOH	[16]
FeS_2/NiS_2	/	10	233	64	1.0 M KOH	[17]
V-NiS_2	0.272	10	290	45	1.0 M KOH	[18]
Co@CoFe-P NBs	0.30	10	266	26.94	1.0 M KOH	[19]
Ni-Fe disulfide@oxyhydroxide	0.126	10	230	42.6	1.0 M KOH	[20]
Ti-CoS_x HSS	0.255	10	245	45.5	1.0 M KOH	[21]
P-doped Ni-Fe-S	0.28	10	264	48	1.0 M KOH	[22]

Table S4: Comparison of long-term stability of OER electrocatalysts in 1.0 M KOH for similar reported systems.

Catalyst	j (mA cm^{-2})	η (mV)	Stability time (hours)	Electrolytes	Ref.
Fe,Ni-CoS_2	**52**	**285**	**500**	**1.0 M KOH**	**This work**
MoO_x/Ni_3S_2	17	230	200	1.0 M KOH	[23]
$CuCo_2S_4$ NS	10	310	12	1.0 M KOH	[24]
Co-S	168	440	20	1.0 M KOH	[25]
Co_9S_8@NOSC	10	340	10	1.0 M KOH	[26]
$NiCo_2S_4$	10	--	30	1.0 M KOH	[27]
CoS-$Co(OH)_2$@MoS_{2+x}	10	380	27.8	1.0 M KOH	[12]
$MnCo_2S_4$ NW	50	--	100	1.0 M KOH	[28]
Zn-Ni_3S_2	52	300	20	1.0 M KOH	[29]
Co_9S_8 NPs/CNS	10	300	10	1.0 M KOH	[30]
Fe_3O_4-Co_3S_4 NS	10	270	24	1.0 M KOH	[31]
S-Co NPs/CNS	10	330	12	1.0 M KOH	[32]
Ni_3S_2 L	22.5	450	12	1.0 M KOH	[11]
NiS@N/S-C	10	420	10	1.0 M KOH	[33]
NiS/Ni foam	20	290	20	1.0 M KOH	[34]
$NiCo_2S_4$ NW/NF	5.5	297	50	1.0 M KOH	[35]

Table S5: Fitting parameters of LCF of Fe,Ni-CoS_2-OCP-CoOOH in-situ system

Fe,Ni-CoS_2	Fe,Ni-CoS_2-Co OCP		CoOOH		R-factor
	Weight	ΔE_0	Weight	ΔE_0	
1.10	0.97	-0.04	0.03	-2.6	0.000025
1.20	0.89	-0.09	0.11	-0.57	0.000089
1.30	0.69	-0.12	0.31	0.04	0.000070
1.40	0.25	-0.16	0.75	0.29	0.000165
1.45	0.15	-0.16	0.85	0.35	0.000210
1.50	0.14	0.29	0.86	0.56	0.000776

Table S6: Fitting parameters of in-situ Co K-edge EXAFS spectra for Fe,Ni-CoS_2 catalyst

	Fe,Ni-CoS_2				
	path	**CN**[a]	**R (Å)**[b]	**ΔEo (eV)**[c]	**σ^2(10^{-3}Å^2)**[d]
OCP	Co – S	5.9 (1)	2.31 (2)	0.48 (2)	4.8 (1)
1.10 V	Co – S	5.8 (2)	2.31 (1)	0.66 (1)	4.7 (2)
	Co – O	0.1 (4)	1.89 (2)		5.0 (1)
1.20 V	Co – S	5.2 (4)	2.32 (1)	0.79 (2)	5.1 (1)
	Co – O	0.6 (1)	1.87 (2)		4.8 (1)
1.30 V	Co – S	3.6 (5)	2.32 (1)	1.80 (1)	5.0 (4)
	Co – O	2.2 (3)	1.89 (3)		5.0 (2)
	Co – $Co_{(CoOOH)}$	2.3 (3)	2.84 (3)		8.9 (3)
1.40 V	Co – S	0.8 (3)	2.33 (2)	-5.40 (2)	2.0 (1)
	Co – O	4.2 (2)	1.89 (4)		5.1 (2)
	Co – $Co_{(CoOOH)}$	3.3 (4)	2.82 (4)		6.3 (4)
1.45 V	Co – S	0.5 (2)	2.35 (1)	-5.97 (3)	5.0 (2)
	Co – O	4.7 (7)	1.89 (5)		4.9 (1)
	Co – $Co_{(CoOOH)}$	3.3 (7)	2.82 (2)		5.0 (1)
1.50 V	Co – S	0.4 (3)	2.33 (2)	-6.1 0(1)	6.8 (2)
	Co – O	4.7 (2)	1.86 (2)		4.5 (3)
	Co – $Co_{(CoOOH)}$	3.6 (4)	2.82 (1)		4.4 (3)

[a] the average coordination number CN (CN was set as the theoretical value during a fitting before OER). [b] Debye-Waller factor σ^2 was set in a range of 0.004 to 0.01. [c] inner potential shift ΔEo was set to equal and in a range of -6 to 6 eV. [d] R is the interatomic distance from the central scattering atom.

References

[1] Hohenberg, P.; Kohn, W. Inhomogeneous electron gas. *Phys. Rev*. **1964**, *136*, B864.

[2] Kresse, G.; Furthmüller, J. Efficient iterative schemes for ab initio total-energy calculations using a plane-wave basis set. *Phys. Rev. B* **1996**, *54*, 11169.

[3] Perdew, J. P.; Burke, K.; Ernzerhof, M. Generalized gradient approximation made simple. *Phys. Rev. Lett*. **1996**, *77*, 3865.

[4] Kresse, G.; Joubert, D. From ultrasoft pseudopotentials to the projector augmented-wave method. *Phys. Rev. B* **1999**, *59*, 1758.

[5] Grimme, S.; Antony, J.; Ehrlich, S.; Krieg, H. A consistent and accurate ab initio parametrization of density functional dispersion correction (DFT-D) for the 94 elements H-Pu. *J. Chem. Phys*. **2010**, *132*, 154104.

[6] Monkhorst, H. J.; Pack, J. D. Special points for Brillouin-zone integrations. *Phys. Rev. B* **1976**, *13*, 5188.

[7] Nørskov, J. K.; Bligaard, T.; Logadottir, A.; Kitchin, J. R.; Chen, J. G.; Pandelov, S.; Stimming, U. Trends in the exchange current for hydrogen evolution. *J. Electrochem. Soc*. **2005**, *152*, J23.

[8] Wang, M.; Dong, C. L.; Huang, Y. C.; Shen, S. Operando spectral and electrochemical investigation into the heterophase stimulated active species transformation in transition-metal sulfides for efficient electrocatalytic oxygen evolution. *ACS Catal.* **2020**, *10*, 1855-1864.

[9] Li, T.; Jing, T.; Rao, D.; Jia, X.; Zuo, Y.; Kment, Š.; Zbořil, R. In situ coating amorphous boride on ternary pyrite-type boron sulfide for highly efficient oxygen evolution. *J. Mater. Chem. A* **2021**, *9*, 12283-12290.

[10] Yu, Z.; Bai, Y.; Zhang, S.; Liu, Y.; Zhang, N.; Sun, K. Metal–organic framework-derived $Zn_{0.975}Co_{0.025}S/CoS_2$ embedded in N, S-codoped carbon nanotube/nanopolyhedra as an

efficient electrocatalyst for overall water splitting. *J. Mater. Chem. A* **2018**, *6*, 10441-10446.

[11] Fan, K.; Zou, H.; Ding, Y.; Dharanipragada, N. A.; Fan, L.; Inge, A. K.; Duan, L.; Zhang, B.; Sun, L. Sacrificial W Facilitates Self-Reconstruction with Abundant Active Sites for Water Oxidation. *Small* **2022**, 2107249.

[12] Yoon, T.; Kim, K. S. One-Step Synthesis of CoS-Doped β-$Co(OH)_2$@Amorphous MoS_{2+x} Hybrid Catalyst Grown on Nickel Foam for High-Performance Electrochemical Overall Water Splitting. *Adv. Funct. Mater.* **2016**, *26*, 7386-7393.

[13] Liu, Y.; Xie, X.; Zhu, G.; Mao, Y.; Yu, Y.; Ju, S.; Shen, X.; Pang, H. Small sized Fe-Co sulfide nanoclusters anchored on carbon for oxygen evolution. *J. Mater. Chem. A* **2019**, *7*, 15851-15861.

[14] Hua, Y.; Jiang, H.; Jiang, H.; Zhang, H.; Li, C. Hierarchical porous CoS_2 microboxes for efficient oxygen evolution reaction. *Electrochim. Acta* **2018**, *278*, 219-225.

[15] Xin, W.; Jiang, W. J.; Lian, Y.; Li, H.; Hong, S.; Xu, S.; Yan, H.; Hu, J. S. NiS_2 nanodotted carnation-like CoS_2 for enhanced electrocatalytic water splitting. *Chem. Commun.* **2019**, *55*, 3781-3784.

[16] Yang, J.; Zhu, G.; Liu, Y.; Xia, J.; Ji, Z.; Shen, X.; Wu, S. Fe_3O_4-decorated Co_9S_8 nanoparticles in situ grown on reduced graphene oxide: a new and efficient electrocatalyst for oxygen evolution reaction. *Adv. Funct. Mater.* **2016**, *26*, 4712-4721.

[17] Jin, J.; Yin, J.; Liu, H.; Xi, P. Synthesis of silk-like FeS_2/NiS_2 hybrid nanocrystals with improved reversible oxygen catalytic performance in a Zn-air battery. *Chinese J. Catal.* **2019**, *40*, 43-51.

[18] Liu, H.; He, Q.; Jiang, H.; Lin, Y.; Zhang, Y.; Habib, M.; Chen, S. M.; Song, L. Electronic structure reconfiguration toward pyrite NiS_2 via engineered heteroatom defect boosting overall water splitting. *ACS nano* **2017**, *11*, 11574-11583.

[19] Zhao, Y.; Dongfang, N.; Triana, C. A.; Huang, C.; Erni, R.; Wan, W.; Li, J.; Stoian, D.; Pan, L.; Zhang, P.; Lan, J.; Iannuzzi, M.; Patzke, G. R. Dynamics and control of active sites in hierarchically nanostructured cobalt phosphide/chalcogenide-based electrocatalysts for water splitting. *Energy Environ. Sci.* **2022**.

[20] Zhou, M.; Weng, Q.; Zhang, X.; Wang, X.; Xue, Y.; Zeng, X.; Bando, Y.; Golberg, D. In situ electrochemical formation of core-shell nickel-iron disulfide and oxyhydroxide heterostructured catalysts for a stable oxygen evolution reaction and the associated mechanisms. *J. Mater. Chem. A* **2017**, *5*, 4335-4342.

[21] Bao, T.; Xia, Y.; Lu, J.; Zhang, C.; Wang, J.; Yuan, L.; Zhang, Y.; Liu, C.; Yu, C. A Pacman-Like Titanium-Doped Cobalt Sulfide Hollow Superstructure for Electrocatalytic Oxygen Evolution. *Small* **2021**, *18*, 2103106.

[22] Lim, D.; Lim, C.; Hwang, M.; Kim, M.; Shim, S. E.; Baeck, S. H. Facile synthesis of flower-like P-doped nickel-iron disulfide microspheres as advanced electrocatalysts for the oxygen evolution reaction. *J. Power Sources* **2021**, *490*, 229552.

[23] Wu, Y.; Li, G. D.; Liu, Y.; Yang, L.; Lian, X.; Asefa, T.; Zou, X. Overall Water Splitting Catalyzed Efficiently by an Ultrathin Nanosheet-Built, Hollow Ni_3S_2-Based Electrocatalyst. *Adv. Funct. Mater.* **2016**, *26*, 4839-4847.

[24] Chauhan, M.; Reddy, K. P.; Gopinath, C. S.; Deka, S. Copper cobalt sulfide nanosheets realizing a promising electrocatalytic oxygen evolution reaction. *ACS Catal.* **2017**, *7*, 5871-5879.

[25] Liu, T.; Liang, Y.; Liu, Q.; Sun, X.; He, Y.; Asiri, A. M. Electrodeposition of cobalt-sulfide nanosheets film as an efficient electrocatalyst for oxygen evolution reaction. *Electrochem. Commun.* **2015**, *60*, 92-96.

[26] Huang, S.; Meng, Y.; He, S.; Goswami, A.; Wu, Q.; Li, J.; Tong, S.; Asefa, T.; Wu, M. N-, O-, and S-tridoped carbon-encapsulated Co_9S_8 nanomaterials: efficient bifunctional electrocatalysts for overall water splitting. *Adv. Funct. Mater.* **2017**, *27*, 1606585.

[27] Jiang, J.; Yan, C.; Zhao, X.; Luo, H.; Xue, Z.; Mu, T. A PEGylated deep eutectic solvent for controllable solvothermal synthesis of porous $NiCo_2S_4$ for efficient oxygen evolution reaction. *Green Chem.* **2017**, *19*, 3023-3031.

[28] Zhang, X.; Si, C.; Guo, X.; Kong, R.; Qu, F. A $MnCo_2S_4$ nanowire array as an earth-abundant electrocatalyst for an efficient oxygen evolution reaction under alkaline conditions. *J. Mater. Chem. A* **2017**, *5*, 17211-17215.

[29] Liu, Q.; Xie, L.; Liu, Z.; Du, G.; Asiri, A. M.; Sun, X. A Zn-doped Ni_3S_2 nanosheet array as a high-performance electrochemical water oxidation catalyst in alkaline solution. *Chem. Commun.* **2017**, *53*, 12446-12449.

[30] Al-Mamun, M.; Wang, Y.; Liu, P.; Zhong, Y. L.; Yin, H.; Su, X.; Zhang, H.; Yang, H.; Wang, D.; Tang, Z.; Zhao, H. One-step solid phase synthesis of a highly efficient and robust cobalt pentlandite electrocatalyst for the oxygen evolution reaction. *J. Mater. Chem. A* **2016**, *4*, 18314-18321.

[31] Du, J.; Zhang, T.; Xing, J.; Xu, C. Hierarchical porous Fe_3O_4/Co_3S_4 nanosheets as an efficient electrocatalyst for the oxygen evolution reaction. *J. Mater. Chem. A* **2017**, *5*, 9210-9216.

[32] Al-Mamun, M.; Zhu, Z.; Yin, H.; Su, X.; Zhang, H.; Liu, P.; Yang, H.; Wang, D.; Teng, Z.; Wang, Y.; Zhao, H. The surface sulfur doping induced enhanced performance of cobalt catalysts in oxygen evolution reactions. *Chem. Commun.* **2016**, *52*, 9450-9453.

[33] Yang, L.; Gao, M.; Dai, B.; Guo, X.; Liu, Z.; Peng, B. An efficient NiS@N/SC hybrid oxygen evolution electrocatalyst derived from metal-organic framework. *Electrochim. Acta* **2016**, *191*, 813-820.

[34] Zhu, W.; Yue, X.; Zhang, W.; Yu, S.; Zhang, Y.; Wang, J.; Wang, J. Nickel sulfide microsphere film on Ni foam as an efficient bifunctional electrocatalyst for overall water splitting. *Chem. Commun.* **2016**, *52*, 1486-1489.

[35] Sivanantham, A.; Ganesan, P.; Shanmugam, S. Hierarchical $NiCo_2S_4$ nanowire arrays supported on Ni foam: an efficient and durable bifunctional electrocatalyst for oxygen and hydrogen evolution reactions. *Adv. Funct. Mater.* **2016**, *26*, 4661-4672.